

Nanosized Monometallic Selenides Heterostructures Implanted into Metal Organic Frameworks-Derived Carbon for Efficient Lithium Storage

Zhichao Liu

Shandong University of Technology

Dong Wang (✉ wangdong2@sdut.edu.cn)

Shandong University of Technology <https://orcid.org/0000-0001-9336-7394>

Hongliang Mu

Shandong University of Technology

Chunjie Zhang

Harbin Institute of Technology

Liqing Wu

Shandong University of Technology

Liu Feng

Shandong University of Technology

Xiuyu Sun

Shandong University of Technology

Guangshuai Zhang

Shandong University of Technology

Jie Wu

Shandong University of Technology

Guangwu Wen

Shandong University of Technology

Research Article

Keywords: heterostructures, monometallic selenides, metal-organic frameworks, lithium-ion batteries, anodes

Posted Date: May 10th, 2021

DOI: <https://doi.org/10.21203/rs.3.rs-500768/v1>

License: © ⓘ This work is licensed under a Creative Commons Attribution 4.0 International License.

[Read Full License](#)

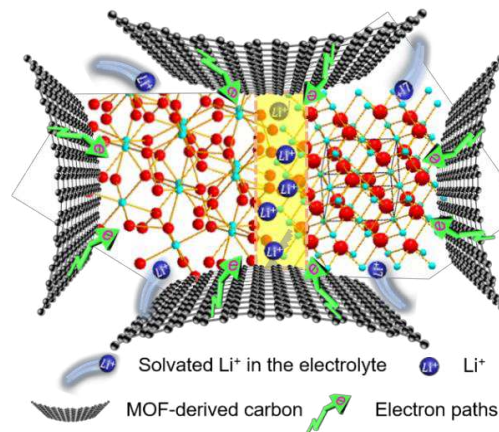
Dear editor,

We would like to submit the enclosed manuscript entitled “**Nanosized Monometallic Selenides Heterostructures Implanted into Metal Organic Frameworks-Derived Carbon for Efficient Lithium Storage**” by Zhichao Liu, Dong Wang,* Hongliang Mu, Chunjie Zhang, Liqing Wu, Liu Feng,* Xiuyu Sun, Guangshuai Zhang, Jie Wu, Guangwu Wen, which we wish to be considered for publication as a “*Research Article*” in *Journal of Advanced Ceramics*. All authors have read and agreed with the submission.

Metal selenides stand out from conversion-type electrodes owing to the weak metal-selenium bond and narrow energy gap, which are kinetically favorable for Li^+ ions insertion/extraction, compared with metal oxides and sulfides. Despite this, metal selenides still suffer from severe volume variation and sluggish Li^+ diffusion kinetics, resulting in capacity fading and inferior rate capabilities. Modulation of electronic structure by engineering heterostructure demonstrates great effectiveness on improving the electrochemical performance of metal selenides. Benefitting from the interfacial charge distribution and lattice distortion at hetero-phase boundaries, the Li^+ ions could be adsorbed easily and transferred swiftly, facilitating reaction kinetics. However, the current selenides heterostructures are largely formed by introducing foreign cations or anions, which makes synthetic process more complex. Moreover, in these heterostructures, heteroatom doping inevitably happen for single selenide component, which could disturb the real insight into the intrinsic mechanism of the performance improvement by two-phase heterostructure. Therefore, it is of great significance to design monometallic selenides heterostructure without any exotic elements and give an in-depth insight into its electrochemical behaviors. Herein, we report the monometallic selenide heterostructures by precisely controlled selenylation of metal-organic frameworks (MOFs) with enhanced lithium storage properties. The main results are highlighted as follows:

- (1) Nanosized monometallic selenide heterostructures that uniformly implanted into porous carbon (i.e., $\text{NiSe/NiSe}_2@\text{C}$, $\text{CoSe/CoSe}_2@\text{C}$) are successfully synthesized via a controlled selenylation of MOFs. Appropriate ratio of MOFs to Se is critical in this synthetic strategy.
- (2) Redistribution of interfacial charge at the two-phase boundaries could promote adsorption and diffusion of Li^+ ions, while the lattice distortions could provide extra active sites. As a result, the monometallic selenide heterostructures showcase improved electron/ions transfer rates and reaction kinetics than single-phase counterparts. As a proof of concept, the $\text{NiSe/NiSe}_2@\text{C}$ manifest excellent electrochemical performance in view of high reversible capacity ($1015.5 \text{ mAh g}^{-1}$

at 0.1 A g⁻¹), good rate capability (500.8 mAh g⁻¹ at 4 A g⁻¹), and long-term cyclic stability.



- (3) Ex-situ XRD, HRTEM, and SAED accompanied with differential capacity versus voltage plots reveal multi-step redox mechanism of the obtained monometallic selenide heterostructures and the reason of conspicuous capacity enhancement.

In this work, monometallic selenide heterostructure are synthesized by controlled selenylation of MOFs, which demonstrate enhanced lithium storage properties to its counterparts. The superiority of monometallic selenide heterostructure with in-depth investigation endow it with great potentials in other energy-related applications. Thus, we think this research is particularly well suited for the broad readerships of *Journal of Advanced Ceramics*.

Finally, this work is original and has not been submitted to or published in any journal. We appreciate your time in reading this article and look forward to hearing from you. Should you have any questions, we will be happy to answer them.

With kind regards,
Sincerely yours,

Dong Wang, Associate Professor,
School of Materials Science and Engineering, Shandong University of Technology,
Zibo, 255000, China,
Email: wangdong2@sdut.edu.cn

Highlights

Nanosized monometallic selenides heterostructure are obtained by precisely controlled selenylation of MOFs.

Rich phase boundaries with interfacial charge redistribution and lattice dislocations promote rapid transfer of electrons and Li^+ ions.

Monometallic selenides heterostructure manifest superior lithium storage properties to the single-phase counterparts.

Nanosized Monometallic Selenides Heterostructures Implanted into Metal Organic Frameworks-Derived Carbon for Efficient Lithium Storage

Zhichao Liu^a, Dong Wang^{a,*}, Hongliang Mu^a, Chunjie Zhang^b, Liqing Wu^a, Liu Feng^{c,*}, Xiuyu Sun^d, Guangshuai Zhang^a, Jie Wu^a, Guangwu Wen^a

^a *School of Materials Science and Engineering, Shandong University of Technology, Zibo 255000, P. R. China.*

^b *School of Materials Science and Engineering, Harbin Institute of Technology, Harbin 150001, P. R. China.*

^c *Analysis and Testing Center, Shandong University of Technology, Zibo 255000, P. R. China.*

^d *School of Chemistry and Chemical Engineering, Shandong University of Technology, Zibo 255000, P. R. China.*

*Corresponding author. School of Materials Science and Engineering, Shandong University of Technology, Zibo 255000, P. R. China.

*Corresponding author. Analysis and Testing Center, Shandong University of Technology, Zibo 255000, P. R. China.

E-mail address: wangdong2@sdut.edu.cn (D. Wang); willow-feng@163.com (L. Feng);

ABSTRACT

Two-phase heterostructure with rich phase boundaries holds great potential in engineering advanced electrode materials. However, current heterostructures are largely generated by introducing exotic cations or anions, complicating synthetic procedures and disturbing real insights into the intrinsic effect of heterostructure. Herein, nanosized monometallic selenides heterostructures are developed by precisely controlled selenylation of metal organic frameworks, which are implanted into in-situ formed carbon (NiSe/NiSe₂@C, CoSe/CoSe₂@C). The disordered atoms arrangement at two-phase boundary leads to the redistribution of interfacial charge and generation of lattice distortions, promoting easy adsorption and swift transfer of Li⁺, and providing extra active sites. As a proof of concept, the NiSe/NiSe₂@C exhibits far surpassing lithium storage properties to single-phase counterparts (NiSe@C and NiSe₂@C), including higher reversible capacity of 1015.5 mAh g⁻¹, better rate capability (500.8 mAh g⁻¹ at 4 A g⁻¹), and superior cyclic performance. As expected, the NiSe/NiSe₂@C manifests lower charge transfer resistance, higher Li⁺ diffusion coefficient, and accelerated capacitive kinetics. Ex-situ X-ray diffraction, high-resolution transmission electron microscopy, and selected area electron diffraction combined with differential capacity versus voltage plots reveal multi-step redox mechanism of NiSe/NiSe₂@C and the reason of conspicuous capacity enhancement. This work demonstrates the enormous potential of monometallic monoanionic heterostructure in energy-related field.

Keywords: heterostructures, monometallic selenides, metal-organic frameworks, lithium-ion batteries, anodes

1. Introduction

Lithium-ion batteries (LIBs) are currently dominant energy storage devices towards commercial requirements owing to the advantages of high energy density, long lifespan, high safety [1,2]. However, the low theoretical capacity of commercial graphite anode limits the further applications of LIBs in electric vehicles and portable electronics [3]. Conversion-type anode materials represented by metal oxides, sulfides, and selenides, have been capturing broad attentions due to their high theoretical capacity and rich reserves [4-6]. Particularly, compared with metal oxides and sulfides, the metal-selenium bonds in selenides are easier to break and interplanar spacing is larger due to the larger radius of selenium atom, which could remarkably promote the kinetics of conversion reaction [7]. Moreover, selenides with narrower energy gap also possess superior electrical conductivity, thus accelerating electrons transportation. Up to now, various selenides including ZnSe [8], NiSe [9], CoSe [10], NiSe₂ [11], have been used as anodes of LIBs. However, the metal selenides still suffer from huge volume variation and sluggish Li⁺ diffusion kinetics during lithiation/delithiation processes, which result in severe structural degradation, capacity fading, and unpromising rate capability [12].

Tremendous efforts have been devoted to circumvent these obstacles of metal selenides, mainly including hybridizing with conductive carbon, geometrical structural regulation, and modulating electronic structure [13]. Notably, modulation of electronic structure by engineering heterogeneous structures demonstrates great effectiveness on improving the electrochemical performance [14,15]. Compared with single-phase metal

selenide, the charge redistribution at the two-phase boundaries in the heterostructure are favorable for the adsorption of ions, thus accelerating reaction kinetics. Moreover, the misaligned arrangement at the heterointerface with rich dislocations, defects, lattice distortions, could improve thermodynamic stability and reaction activity, resulting in improved electrochemical performance. For example, Fang et al. reported that the heterogeneous interface in the $\text{CoSe}_2/\text{ZnSe}$ could dramatically improve the ions adsorption ability through theoretical calculations and experimental results [16]. Chen et al. demonstrated that $\text{SnSe}/\text{SnO}_2@\text{graphite}$ possesses higher electron mobility and reversible capacity than $\text{SnO}_2@\text{graphite}$, benefitting from the built-in electric field of the SnSe/SnO_2 heterostructure, which delivers a high reversible capacity of 810 mAh g^{-1} after 200 cycles [17]. However, previously reported selenides-based heterostructures were generally formed through introducing exotic anions or cations to generate two distinct phases, which complicated the preparation processes with high cost. Moreover, the introduction of foreign atoms always gives rise to element-doping into single selenide component, which could disturb the real insight into the intrinsic mechanism of the performance improvement by the two-phase heterostructure. In this regard, an in-depth research on the monometallic selenides heterostructure could provide straightforward insight into the role of two-phase heterojunction on the electrochemical performance, and also advance better exploitation and practical application of other heterostructures. In addition, the preparation of monometallic selenide heterostructures using metal organic framework (MOF) as the precursor could inherit its porous characteristics, thus providing rich channels for electrolyte infiltration

and Li^+ ions diffusion. Moreover, the in-situ formed carbon skeleton also improve the conductivity of the material and restrict the agglomeration of active nanocrystals [18].

In this work, we reported the MOF-engaged synthesis of nanosized monometallic selenide heterostructure embedded into in-situ formed carbonaceous matrix (i.e., $\text{NiSe/NiSe}_2@\text{C}$ and $\text{CoSe/CoSe}_2@\text{C}$), by accurate ratio regulation of MOF to Se. Taken $\text{NiSe/NiSe}_2@\text{C}$ as an illustrative example, abundant phase boundaries with lattice dislocations and defects between NiSe and NiSe_2 domains were verified, while the X-ray photoelectron spectroscopy (XPS) and Raman proved the interfacial charge redistribution inside the heterostructure, which could promote rapid adsorption and swift transfer of Li^+ ions at the heterointerfaces. As expected, the as-synthesized $\text{NiSe/NiSe}_2@\text{C}$ shows enhanced lithium storage properties than the $\text{NiSe}@\text{C}$ and $\text{NiSe}_2@\text{C}$ in view of higher reversible capacity (1015.5 mAh g^{-1} after 100 cycles at 0.1 A g^{-1} ; $\text{NiSe}@\text{C}$: 591.3 mAh g^{-1} ; $\text{NiSe}_2@\text{C}$: 529.7 mAh g^{-1}), better rate capability (500.8 mAh g^{-1} at 4 A g^{-1} ; $\text{NiSe}@\text{C}$: 333.3 mAh g^{-1} ; $\text{NiSe}_2@\text{C}$: 277.9 mAh g^{-1}), and stable cyclic performance (540.3 mAh g^{-1} after 1000 cycles). Electrochemical analyses demonstrated that the $\text{NiSe/NiSe}_2@\text{C}$ manifests accelerated diffusion kinetics of Li^+ ions and more favored pseudocapacitance contribution. Ex-situ X-ray diffraction (XRD) together with ex-situ high-resolution transmission electron microscopy (HRTEM) and selected area electron diffraction (SAED) reveal the multi-step reaction mechanism and structural evolution of the $\text{NiSe/NiSe}_2@\text{C}$ during lithiation/delithiation processes. Furthermore, the differential capacity versus voltage plots discloses the increased utilization of selenides heterostructure upon cycling, and reversible generation and

decomposition of polymeric-gel film owing to gradual electrode activation. As another proof of concept, the CoSe/CoSe₂@C also showcase superior reversible capacity, rate capability, and cyclic performance to its counterparts.

2. Experimental

2.1 Materials preparation

Preparation of Ni-MOF: All chemicals are of analytical grade and were directly used without further purification. Typically, Ni(CH₃COO)₂ • 4H₂O (0.3732g, 1.5 mmol) was dissolved in deionized water (20 ml) and ethanol (20 ml), and then PVP (*M_w*=10000, 10 g) was added into the above solution with continuously stirring for 30 min to form solution A. Trimesic acid (0.4518g, 2.15 mmol) was added to a mixed solvent with deionized water (20 ml) and ethanol (20 ml) to form another clear solution B. Then, solution B was quickly poured into solution A, and the obtained solution was maintained at room temperature for 24 h after stirring for 30 minutes. Finally, the green precipitate named Ni-MOF was collected by centrifugation, washed repeatedly with ethanol, and thoroughly dried under vacuum for further use.

Preparation of NiSe/NiSe₂@C: The Ni-MOF precursor and Se powder were thoroughly ground and mixed in an agate mortar with mass ratio of 3:2. Then, the mixture was annealed at 450 °C for 2 h in Ar atmosphere with a heating rate of 1 °C min⁻¹. After cooling down to room temperature, the NiSe/NiSe₂@C product was obtained. The preparation processes of the NiSe@C and NiSe₂@C were identical to that of NiSe/NiSe₂@C except for the mass ratio of Ni-MOF precursor to Se powder. For the NiSe@C, the mass ratio of Ni-MOF: Se was 3:1, while for the NiSe₂@C, the

mass ratio of Ni-MOF: Se was 3:3.

Preparation of CoSe@C, CoSe/CoSe₂@C, and CoSe₂@C: The preparation procedures of CoSe@C, CoSe₂@C, and CoSe/CoSe₂@C were similar to those of NiSe@C, NiSe₂@C, and NiSe/NiSe₂@C except that Ni(CH₃COO)₂·4H₂O was replaced by Co(CH₃COO)₂·4H₂O. For CoSe@C, the mass ratio of Co-MOF precursor: Se was 3:1. For CoSe/CoSe₂@C, the mass ratio of Co-MOF precursor: Se was 3:2. For CoSe₂@C, the mass ratio of Co-MOF precursor: Se was 3:3.

2.2 Materials characterization

The crystal structure of the as-prepared samples was characterized by XRD on a D/MAX-IIIIC with Cu K α radiation at 30 kV and 20 mA. For the semi-quantitative analysis, the scanning range is 10-90°, the scanning step is 0.02°, and the dwell time is 3 s. Scanning electron microscopy (SEM; Sirion 200 FEI Netherlands) was used to characterize the surface morphology of the sample. Transmission electron microscope (TEM), HRTEM, and energy dispersive X-ray spectroscopy (EDS) analysis were carried out on a JEM-2100 microscope to analyze the microstructure of the products. XPS (ESCALAB 250XI) was performed to examine the surface electronic state and chemical valences of the samples. Raman spectra were collected using a Renishaw Invia Raman microscope. The specific surface area was calculated by using Brunauer-Emmett-Teller (BET) and pore diameter distribution plot were obtained by the N₂ adsorption/desorption isotherms on a JWGB, JW-BK200C tester.

2.3 Electrochemical measurement

The electrochemical performance of the obtained samples was assessed based on

CR2032-type coin cells. To prepare the working electrode, 70 wt % active material, 20 wt % acetylene black, and 10 wt % polyvinylidene fluoride (PVDF) were mixed and stirred in N-methyl pyrrolidone (NMP) to form a homogeneous slurry. Then, the slurry was coated onto a copper foil and dried in a vacuum oven at 110 °C for 24 h. The mass loading of the active material was $\sim 1.0 \text{ mg cm}^2$. The coin cells were assembled in an Ar-filled glove box with lithium foil as the reference and counter electrodes, Celgard 2400 membrane as the separator, and 1.0 M LiPF_6 in a mixture of ethylmethyl carbonate (EC)/dimethyl carbonate (DMC)/ethylene carbonate (EMC) (volume ratio of 1:1:1) as the electrolyte. A CHI660B electrochemical workstation (Chen Hua, Shanghai, China) was used to test Cyclic voltammetry (CV: scanning speed: 0.1 mV s^{-1} , voltage window: 0.01-3.0 V) and Electrochemical impedance spectroscopy (EIS: frequency: 0.01- 10^5 Hz). Galvanostatic charge/discharge tests were carried out on the Neware-5v10mA battery system apparatus (voltage window: 0.01-3.0 V) at different current densities.

3. Results and discussion

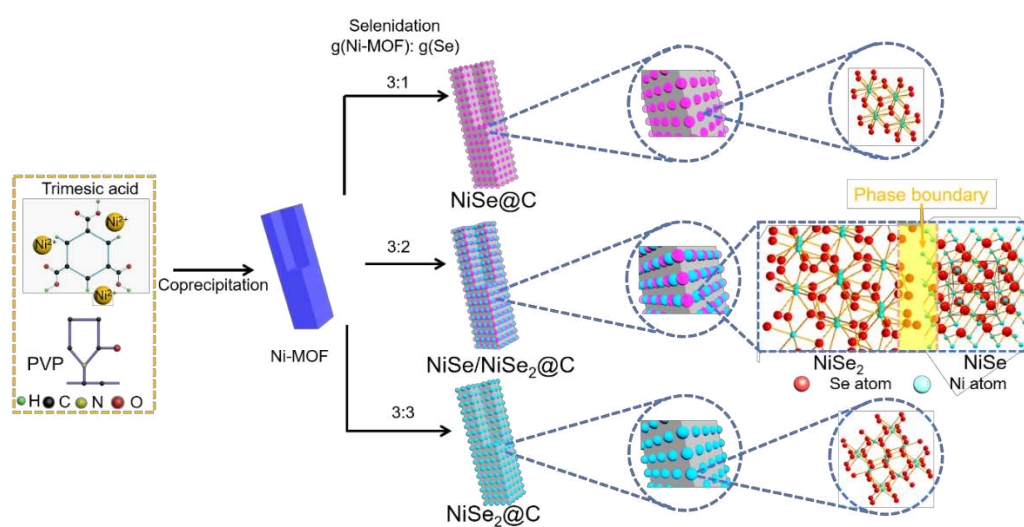


Fig. 1. Schematic illustration for the preparation process of the NiSe@C, NiSe/NiSe₂@C, and NiSe₂@C.

Taken NiSe/NiSe₂@C as an example, the synthetic process of the monometallic selenides heterostructure is schematically illustrated in Fig. 1. Rod-like Ni-MOF precursor (Fig. S1, Supporting Information) was first synthesized through an incubation process at ambient temperature, during which the co-precipitation between Ni²⁺ ions and trimesic acid occurred. Then, the Ni-MOF was converted into nanosized selenides implanted into porous carbon skeleton via a facile selenylation process with Se. Note that the amount of Se powder plays a critical role on obtaining the heterojunction NiSe/NiSe₂. Specifically, the NiSe/NiSe₂@C was obtained with Ni-MOF: Se of 3:2 by weight. On the other hand, when the mass ratios were 3:1 and 3:3, the NiSe@C and NiSe₂@C were generated, respectively.

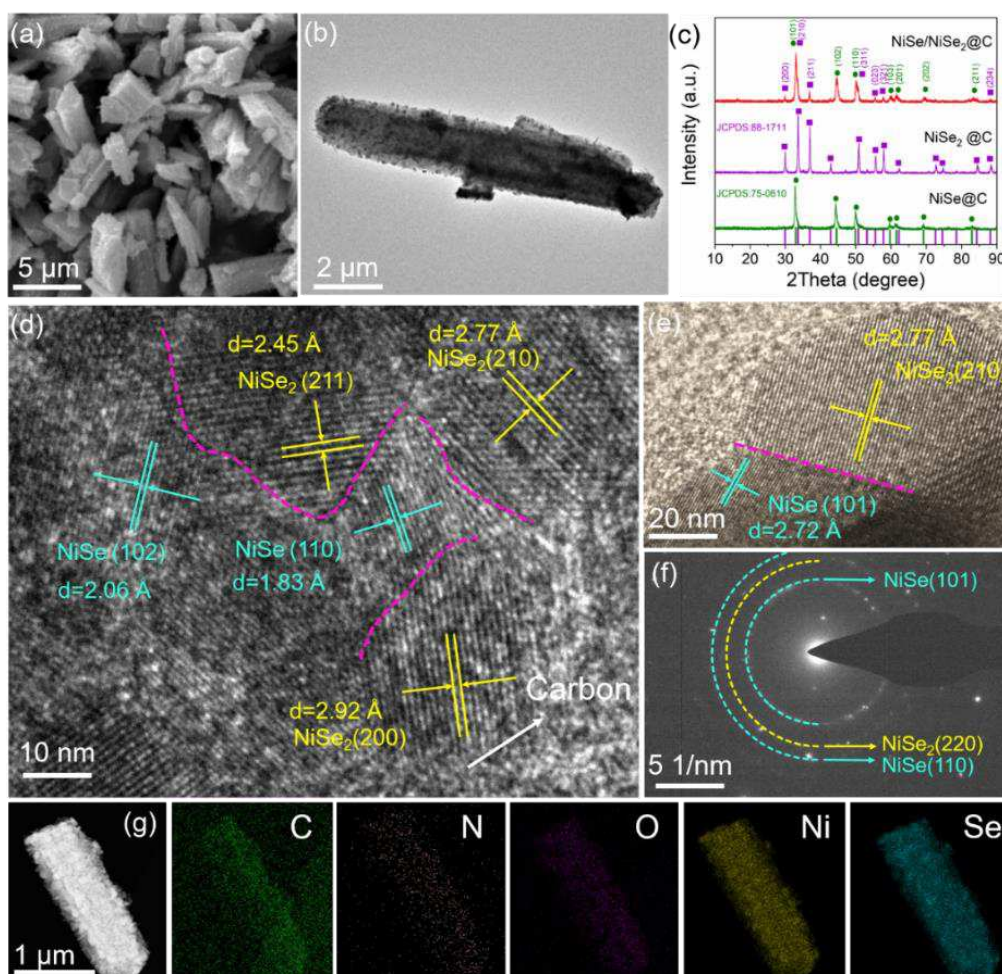


Fig. 2. Material characterization. (a) SEM and (b) TEM images of the NiSe/NiSe₂@C. (c) XRD patterns of the NiSe/NiSe₂@C, NiSe@C, and NiSe₂@C. (d, e) HRTEM images, (f) SAED pattern, (g) HAADF-STEM and elemental mappings images (Ni, Se, C, N, O) of the NiSe/NiSe₂@C.

SEM and TEM images show that the as-obtained NiSe/NiSe₂@C well inherits the rod-like morphology of the Ni-MOF precursor but with much rough surface, which should be ascribed to the decomposition of organic component from Ni-MOF and the permeation of selenium atoms (Fig. 2a and b). Moreover, TEM analysis also demonstrates that the heterostructure nanocrystals are uniformly embedded into the in-situ formed carbon skeleton. XRD measurement was performed to analyze the phase composition of the as-prepared products. As shown in Fig. 2c, the diffraction peaks of the NiSe/NiSe₂@C are identified to hexagonal NiSe (JCPDS No. 5-0610, space group P63/mcc) and cubic NiSe₂ (JCPDS No. 88-1777, space group Pa-3(205)). No diffraction peaks of impurities are detected, suggesting the successful generation of high-quality NiSe/NiSe₂ heterostructure. Semi-quantitative analysis shows that the weight ratio of NiSe to NiSe₂ in the product is about 11:9 (Fig. S2, Supporting Information). In addition, XRD patterns also confirm that pure-phase NiSe and NiSe₂ are respectively obtained with mass ratios of Ni-MOF: Se as 3:1 and 3:3. HRTEM measurements were further implemented to reveal the two-phase property of the NiSe/NiSe₂@C. The lattice fringes with an interplanar distance of 2.06, 2.72, and 1.83 Å match the (102), (101), and (110) crystallographic planes of NiSe, respectively, while the well-defined lattice fringes of 2.45, 2.92, and 2.77 Å should belong to the (211), (200), and (210) planes of NiSe₂, respectively (Fig. 2d, e). As a result, abundant phase boundaries with rich lattice mismatches and distortions are generated between these

nanosized two-phase heterostructures, which could create a large amount of crystal defects and extra accessible active sites for Li^+ ions storage [19]. SAED pattern (Fig. 2f) further confirms the co-existence of NiSe and NiSe₂ in the NiSe/NiSe₂@C, of which the diffraction rings should be assigned to (101), (110) planes of NiSe and (220) plane of NiSe₂. High-angle annular dark-field scanning TEM (HAADF-STEM) and elemental mapping images (Fig. 2g) demonstrate the uniform distribution of C, N, O, Ni, and Se elements, indicating that the NiSe/NiSe₂ domains are homogeneously embedded into N, O-codoped carbon matrix, owing to the one-step carbonization and selenylation of Ni-MOF. These nanosized heterostructures surrounded by in-situ generated porous carbon framework could not only favor for rapid electron/ions transfer but also release the internal stress induced by lithiation/delithiation processes. In addition, detailed morphological and structural characterizations of the NiSe@C and NiSe₂@C are shown in Fig. S3 and S4 (Supporting Information). The N₂ adsorption-desorption isotherms of the NiSe/NiSe₂@C illustrate typical IV-type characteristics with hysteresis loop at medium-high relative pressure and rapid adsorption at low relative pressure, indicating the existence of mesopores and micropores (Fig. S5a, Supporting Information). The BET surface area of the NiSe/NiSe₂@C is calculated to be 53.5 m² g⁻¹, and the pore size distribution obtained according to Barrett–Joyner–Halenda (BJH) method also demonstrates mesoporous structure (Fig. S5b, Supporting Information). The large specific surface area with abundant pores provides the NiSe/NiSe₂@C with enormous electrochemically active sites and sufficient penetration channels for electrolyte during charge/discharge processes, which are beneficial for

improving electrochemical reaction kinetics.

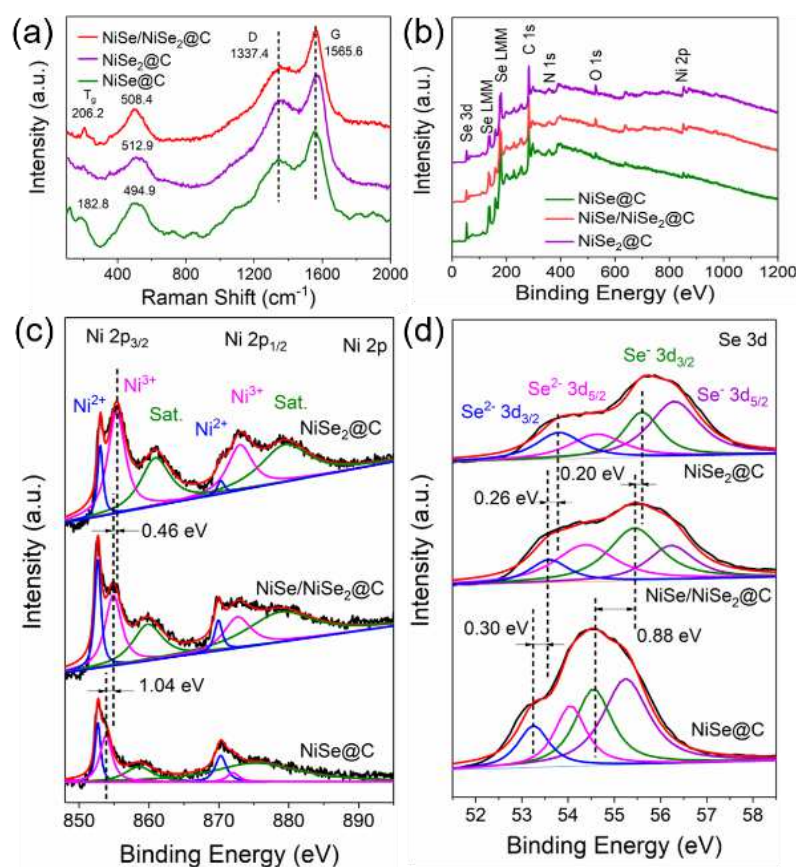


Fig. 3. Material characterization. (a) Raman spectra of the NiSe/NiSe₂@C, NiSe@C, and NiSe₂@C. (b) The survey XPS spectra of the NiSe/NiSe₂@C, NiSe@C, and NiSe₂@C. (c) Comparison of high-resolution Ni 2p XPS spectra for the NiSe/NiSe₂@C and NiSe@C, and for the NiSe/NiSe₂@C and NiSe₂@C. (d) Comparison of high-resolution Se 3d XPS spectra for the NiSe/NiSe₂@C and NiSe@C, and for (f) the NiSe/NiSe₂@C and NiSe₂@C.

Raman and XPS measurements were further performed to verify the formation of two-phase heterostructure in the obtained products. As shown in Fig. 3a, the Raman spectrum of the NiSe/NiSe₂@C shows two characteristic peaks at about 206.2 and 508.4 cm⁻¹, which should belong to the stretching mode of Se-Se pairs (T_g) of NiSe₂ and the longitudinal optical (LO) one-phonon (1P) mode of NiSe, respectively [20-22]. Notably, the peak for the NiSe/NiSe₂ at 508.4 cm⁻¹ slightly shift to higher wavenumbers compared with that for pure NiSe, which should be owing to an opposite charge transfer

induced by the heterogeneous interfaces between NiSe₂ and NiSe phases [23,24]. In addition, the two peaks at about 1337.4 and 1565.6 cm⁻¹ belong to D-band (disordered graphitic carbon) and G-band (sp²-bonded carbon) of the MOFs-derived carbon, respectively [25]. The elemental composition and surface electronic states of the NiSe/NiSe₂@C, NiSe@C, and NiSe₂@C were further analyzed by XPS. It can be seen that these materials all contain anticipated elements, *i.e.*, C, N, O, Ni, and Se (Fig. 3b), consistent with the elemental mapping results. For the NiSe/NiSe₂@C, the high-resolution Ni 2p spectrum can be deconvoluted into two core-level peaks at 852.66 eV (2p_{3/2}) and 869.94 eV (2p_{1/2}), accompanied with their satellite peaks located at 859.89 and 879.16 eV, corresponding to Ni²⁺, while the peaks located at 854.86 (2p_{3/2}) and 872.76 (2p_{1/2}) are assigned to Ni³⁺ (Table S1, Supporting Information) [26]. Notably, it can be observed that the peaks of Ni 2p in NiSe/NiSe₂@C are positively shifted (~1.04 eV) compared with that in NiSe@C, which are negatively (~0.46 eV) shifted compared with that in NiSe₂@C, suggesting strong electronic interaction between NiSe₂ and NiSe phases induced by the electrons transfer from NiSe to NiSe₂ (Fig. 3c) [27,28]. Fig. 3d display the high-resolution Se 3d spectra of the three samples. For the NiSe/NiSe₂@C, the two peaks located at 53.56 eV and 54.36 eV should be attributed to Se²⁻ 3d_{3/2} and Se²⁻ 3d_{5/2}, respectively, while the two peaks at 55.45 eV and 56.25 eV respectively correspond to Se⁻ 3d_{3/2} and Se⁻ 3d_{5/2} (Table S2, Supporting Information) [29]. Obviously, the Se 3d spectra in NiSe/NiSe₂@C exhibit significantly positive shift (~0.30 eV for Se²⁻ and ~0.88 eV for Se⁻) compared with NiSe@C and slightly negative shift (~0.26 eV for Se²⁻ and 0.20 eV for Se⁻) compared with NiSe₂@C, again indicating interfacial

interaction at the heterogeneous boundary and the establishment of strong coupled interface [30]. The electrons transfer from NiSe to NiSe₂ is induced by the lattice defect and distortions at two-phase boundary and could cause interfacial charge redistribution, which are beneficial for Li⁺ ions transportation and improved reaction kinetics [16,31]. Apart from Se and Ni, the C 1s, N 1s, and O 1s spectra were also scanned in high-resolution (Fig. S6, Supporting Information). The corresponding results unveil that the MOF-derived carbon matrix is codoped by N and O species, which are beneficial for improving the conductivity and electrochemical activity of carbon.

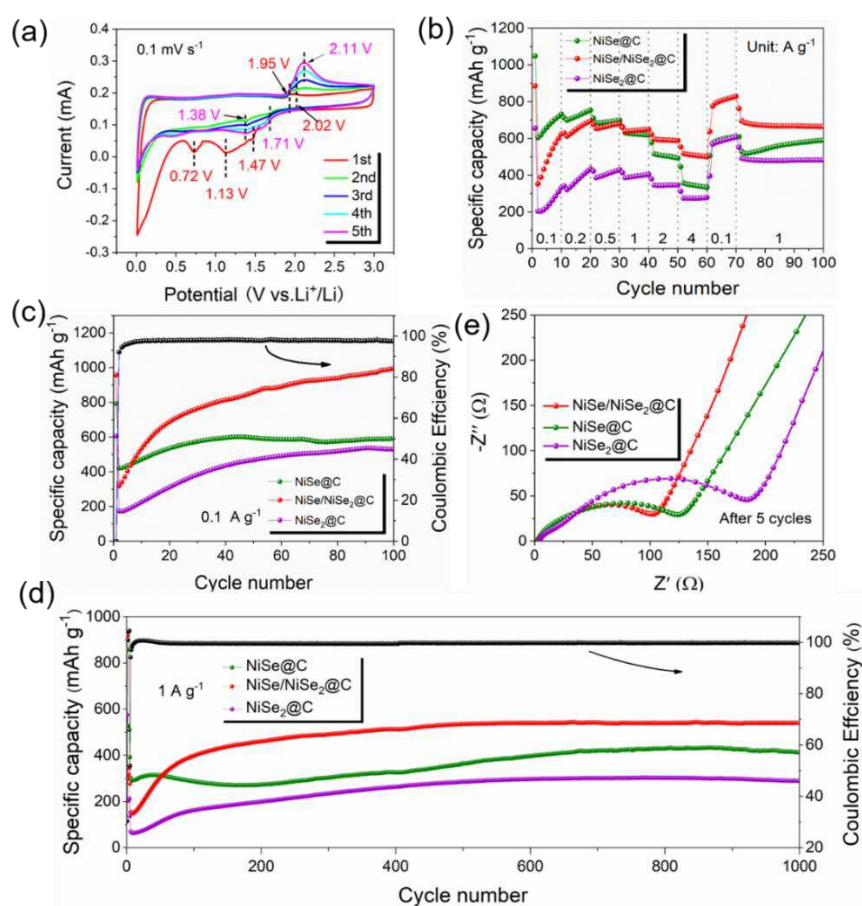


Fig. 4. Lithium storage properties. (a) First five CV curves of the NiSe/NiSe₂@C at 0.1 mV s⁻¹. (b) Rate capabilities of the NiSe/NiSe₂@C, NiSe@C, and NiSe₂@C. Cyclic performance of the NiSe/NiSe₂@C, NiSe@C, and NiSe₂@C at (c) 0.1 A g⁻¹ and (d) 1 A g⁻¹. (e) Nyquist plots of the NiSe/NiSe₂@C, NiSe@C, and NiSe₂@C after 5 charge/discharge cycles.

The lithium storage properties of these three samples were evaluated in half-cell configuration. Fig. 4a and S7 (Supporting Information) show the initial five CV curves of the NiSe/NiSe₂@C, NiSe@C, and NiSe₂@C with a voltage range of 0.01-3.0 V and a scan rate of 0.1 mV s⁻¹. In the first scan of NiSe/NiSe₂@C, two cathodic peaks appear at 1.47 and 1.13 V, which correspond to the orderly reduction of NiSe₂ and NiSe to metallic Ni⁰ as well as the formation of Li₂Se [32]. In addition, the cathodic peak at 0.72 V, which disappears in subsequent cycles, belongs to the irreversible formation of solid-electrolyte interface (SEI) film [33]. During the anodic process, the two peaks at 1.95 and 2.02 V should be assigned to the regeneration of NiSe and NiSe₂, respectively. In the subsequent scans, the cathodic peaks shift from 1.13 and 1.47 V to 1.38 and 1.71 V, respectively, while the anodic peaks deviate slightly to 2.11 V, which should be ascribed to microstructural rearrangement [34]. For comparison, the typical CVs of the NiSe@C and NiSe₂@C electrodes are also demonstrated in Fig. S7, from which it can be observed that the CV curves of the NiSe/NiSe₂@C electrode exhibit combined features of NiSe@C and NiSe₂@C. Specifically, the different redox potentials of NiSe and NiSe₂ lead to ordinal reactions of NiSe₂ and NiSe. Thus, the uniform distribution of NiSe domains in the NiSe/NiSe₂@C could restrict the agglomeration and volume variation of NiSe₂ nanodomains during conversion process. Moreover, the initially formed Li₂Se matrix together with electrically conductive Ni nanonetwork in return provides a buffer function on the conversion reaction of NiSe. Therefore, due to the different lithiation/delithiation potentials of the NiSe₂ and NiSe phases, a synergistic effect that mutually buffers the volume expansion of each other and enhancing electrons

transfer is generated, thus beneficial for combining the advantages of the heterogeneous selenides.

The rate capabilities of the three samples at various current densities are demonstrated in Fig. 4b. It can be seen that the NiSe/NiSe₂@C manifest much higher reversible capacity than the two counterparts, delivering capacities of 624.1, 649.1, 681.2, 649.9, 588.6, and 500.8 mAh g⁻¹ as the current rates increase from 0.1 to 4 A g⁻¹. When the current density returns back to 0.1 A g⁻¹, the capacity recovers to 829.2 mAh g⁻¹, indicating the superb electrochemical reversibility and excellent rate capability of the NiSe/NiSe₂@C. The lower capacities of the NiSe/NiSe₂@C in the initial several cycles than that of NiSe@C might be ascribed to smaller specific surface area of NiSe/NiSe₂@C (Fig. S8, Supporting Information), since larger surface area could provide more surface-active sites for Li⁺ storage. As shown in Fig. 4c, an impressive reversible capacity of 1015.5 mAh g⁻¹ is obtained after 100 cycles for NiSe/NiSe₂@C, far exceeding those of NiSe@C (591.3 mAh g⁻¹) and NiSe₂@C (529.7 mAh g⁻¹). The superior Li⁺ storage properties of NiSe/NiSe₂@C could be attributed to the abundant phase boundaries with distortions and defects inside the NiSe/NiSe₂ heterostructure, which could facilitate the adsorption and transfer of Li⁺ ions and thus improve reaction kinetics. The long-term cyclic performance of NiSe/NiSe₂@C at 1 A g⁻¹ is presented in Fig. 4d with the initial four cycles tested at 0.1 A g⁻¹ to activate the electrode material. Obviously, the NiSe/NiSe₂@C surpass other two materials in terms of reversible capacity and cyclic stability, delivering a substantial value of 540.3 mAh g⁻¹ after 1000 cycles. More significantly, the cyclic performance of NiSe/NiSe₂@C is

also superior to most of previously reported selenide-based electrodes (Table S3, Supporting Information).

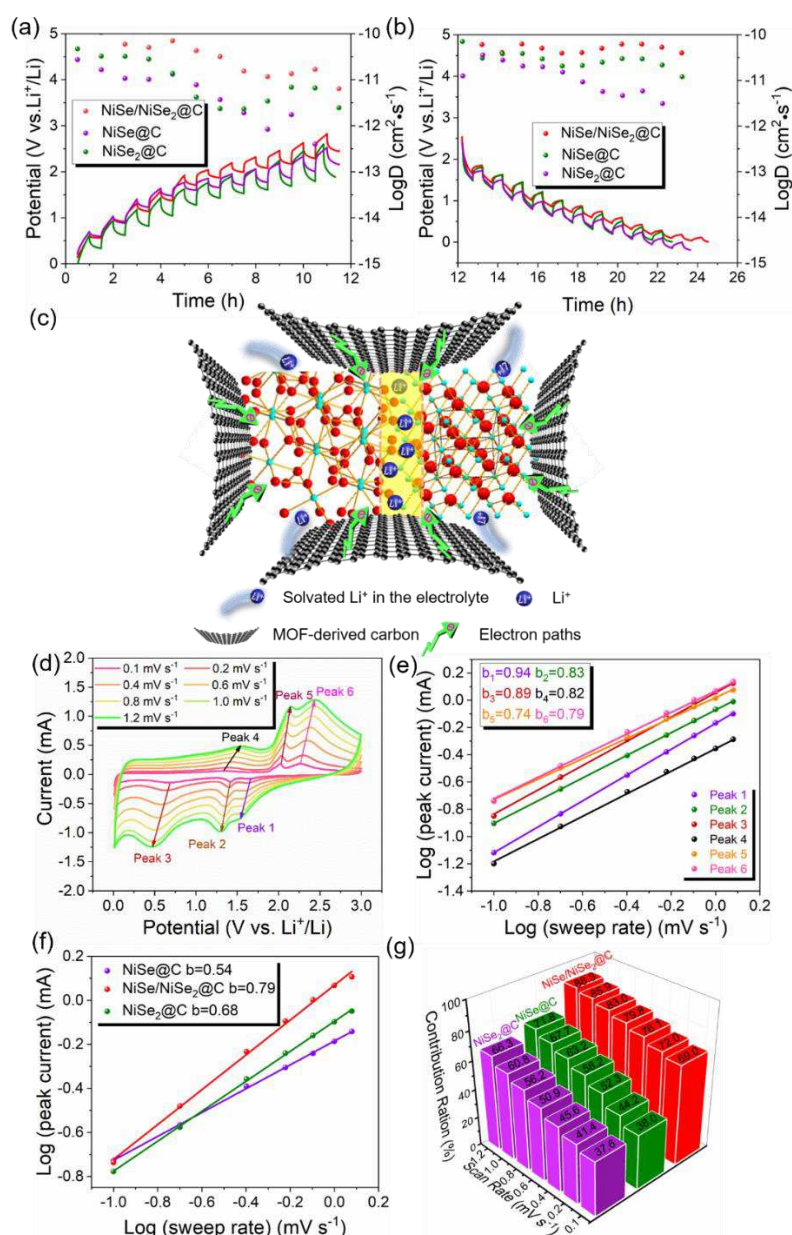


Fig. 5. Kinetics analyses. GITT curves and corresponding Li⁺ ions diffusion coefficients of the NiSe/NiSe₂@C, NiSe@C, and NiSe₂@C electrodes during (a) the 10st discharge process and (b) the 10st charge process. (c) Schematic illustration for the charge storage of the NiSe/NiSe₂@C. (d) CV curves of the NiSe/NiSe₂@C at various scan rates from 0.1 to 1.2 mV s⁻¹ after 5 charge/discharge cycles. (e) Linear relationship between log (*i*) and log (*v*) of the NiSe/NiSe₂@C. (f) Comparison of *b* values among the NiSe/NiSe₂@C, NiSe@C, and NiSe₂@C electrodes. (g) The percentage of capacitive contributions at different scan rates of the NiSe/NiSe₂@C, NiSe@C, and NiSe₂@C electrodes.

To gain an in-depth insight into the enhanced electrochemical performance of NiSe/NiSe₂@C, EIS and galvanostatic intermittent titration technique (GITT) measurements were performed to evaluate the Li⁺/electrons transfer behaviors during charge/discharge processes. Fig. 4e compares the Nyquist plots of the NiSe/NiSe₂@C, NiSe@C, and NiSe₂@C electrodes after five cycles. Based on the equivalent circuit (Fig. S9, Supporting Information), the charge transfer resistance (R_{ct}) of NiSe/NiSe₂@C (94 Ω) is much smaller than those of NiSe@C (146 Ω) and NiSe₂@C (215 Ω), suggesting higher charge transfer kinetics along the electrode/electrolyte interface. Then, the diffusion coefficients of Li⁺ ions were measured by GITT, which could be calculated according to the simplified formula as follow [35]

$$D = \frac{4L^2}{\pi\tau} \left(\frac{\Delta E_s}{\Delta E_t} \right)^2 \quad (1)$$

where τ is the relaxation time (s), ΔE_s is the change of potential (V) caused by the current pulse, ΔE_t represents the change of potential (V) during the constant current pulse after eliminating iR drop, L stands for the length of the lithium-ion diffusion path (cm), which could be simplified as the electrode thickness (Fig. S10, Supporting Information). Fig. 5a and b show that the Li⁺ ions diffusion coefficients of the three electrodes vary during the charge/discharge processes. Apparently, the NiSe/NiSe₂@C showcase higher Li⁺ ions diffusion coefficient and minor fluctuant than each single-phase selenide, demonstrating that the NiSe/NiSe₂ heterostructure facilitates rapid transfer of Li⁺ ions and thus improves reaction kinetics. As illustrated in Fig. 5c, the engineering of nanosized NiSe/NiSe₂ heterostructures can generate phase boundaries

with rich lattice twist, distortions, and mismatches for thermodynamic stability, which could provide extra accessible active sites for Li⁺ ions capture. Moreover, the charge rearrangement at the heterojunction interfaces could decrease the adsorption energy of ions, thus accelerating reaction kinetics and electrochemical activity. In addition, the robust and porous carbon matrix as scaffold greatly restrains the volume expansion and agglomeration of the NiSe/NiSe₂ heterostructures during Li⁺ insertion/extraction, as well as improves the overall electronic conductivity of the material.

To further investigate the effects of NiSe/NiSe₂ heterostructure on reaction kinetics and charge storage mechanism, CV measurements at various scan rates from 0.1 to 1.2 mV s⁻¹ were carried out for these three electrodes after several charge/discharge cycles (Fig. 5d and Fig. S11a, c, Supporting Information). As the scan rate increases, the CVs of NiSe/NiSe₂@C present similar shapes and slightly shifted peaks. Generally, the total charge storage of electrode consists of surface-induced capacitive contribution and diffusion-dominated faradaic region, while the peak current (*i*) and scan rate (*v*) comply with the formulas below [36]

$$i = av^b \quad (2)$$

$$\log(i) = b \log(v) + \log(a) \quad (3)$$

where *a* and *b* are two variable parameters. The *b* value could be calculated by the slope of the log(*i*)-log(*v*) plot, while *b*=0.5 represents the diffusion-controlled process and *b*=1.0 suggest capacitive behaviors [37]. There are six major redox peaks during the charge/discharge processes, and their corresponding *b* values are 0.94, 0.83, 0.89, 0.82, 0.74, 0.79, telling us that the total Li⁺ storage capacity of NiSe/NiSe₂@C is contributed

by the capacitive-dominated and diffusion-controlled process simultaneously (Fig. 5e). The NiSe@C and NiSe₂@C electrode also showcase similar charge storage behaviors (Fig. S11b, d, Supporting Information). However, the NiSe/NiSe₂@C manifests higher *b* values than the NiSe@C and NiSe₂@C (Fig. 5f), suggesting a more favored capacitive kinetics of NiSe/NiSe₂@C. The surface-induced capacitive contribution could be further quantified by the following formula [38]

$$i(V)=k_1v + k_2v^{0.5} \quad (4)$$

where *i*(V) is the total current response at a given potential V and *v* represents the scan rate. By determining the *k*₁ values, the fraction of the capacitive current (*k*₁*v*) can be distinguished from the Li⁺ diffusion contribution (*k*₂*v*^{0.5}). Fig. 5g compares the capacitance contribution to the total capacity for the three samples at various scan rates, which increases gradually as the sweep speeds increase from 0.1 to 1.2 mV s⁻¹. Specifically, the surface capacitive contributions are 69.0 %, 72.0 %, 76.1 %, 79.8 %, 83.0 %, 85.9 %, 88.3 % at 0.1, 0.2, 0.4, 0.6, 0.8, 1.0, and 1.2 mV s⁻¹, respectively, for the NiSe/NiSe₂@C electrode. Obviously, the ratios of capacitive effects on the NiSe/NiSe₂@C are much higher than those of the other two electrodes at all scan rates. It is worth noting that more capacitive behavior benefits for fast reaction kinetics and stable cyclic performance especially at high rate [39]. Hence, the high capacitive contribution for the NiSe/NiSe₂@C electrode is consistent with its superior rate capability and cyclic stability.

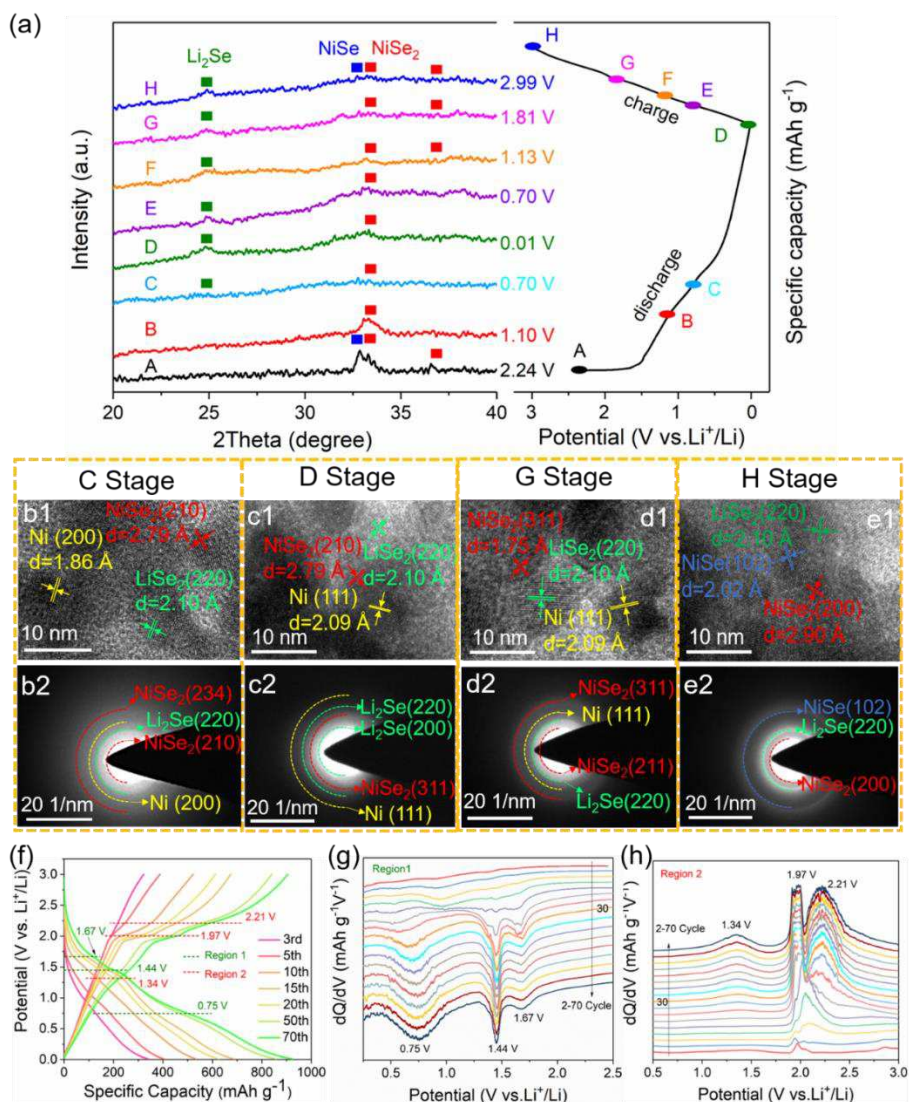


Fig. 6. Electrochemical reaction mechanism. (a) Ex-situ XRD patterns collected at different cut-off voltages, corresponding to the charge/discharge curves. Ex-situ HRTEM images and corresponding SAED patterns of the NiSe/NiSe₂@C electrode at C stage (b1-b2), D stage (c1-c2), G stage (d1-d2), and H stage (e1-e2) during the first cycle. (f) Representative charge–discharge voltage profiles of the NiSe/NiSe₂@C electrode with corresponding differential capacity versus voltage plots at (g) region 1 (discharge) and (h) region 2 (charge).

In order to unveil the electrochemical reaction mechanism of the NiSe/NiSe₂@C, ex-situ XRD together with ex-situ TEM, HRTEM and SAED measurements were performed to examine the evolution of crystalline structure during charge/discharge. According to the slow-sweep CV curve at 0.01 mV s⁻¹, the initial lithiation/delithiation

processes of the NiSe/NiSe₂@C is divided based on eight stages (stages A-H in Fig. S12, Supporting Information). During the first discharge process, the diffraction peaks of the original electrode (Fig. 6a, stage A) belong to NiSe (32.8°) and NiSe₂ (33.5° and 36.8°). As the potential decreases to 1.10 V (stage B), the diffraction peaks of NiSe at 32.8° and NiSe₂ at 36.8° disappear due to the conversion reaction of NiSe and partial NiSe₂ with Li⁺ ions as depicted in equations 5 and 6. As the discharge continues to 0.01 V (stage D), new diffraction peak around 25.7° is detected with enhanced intensities, which is indexed to the discharge product of cubic Li₂Se. In addition, a weak peak at 33.5° belonging to NiSe₂ is saved probably due to incomplete utilization. No diffraction peaks of metallic Ni⁰ are observed at the fully discharged state, which might be ascribed to its ultrafine or amorphous feature [40]. To confirm the aforementioned structural evolution of the electrode, HRTEM and SAED patterns were collected at stages C and D (Fig. 6b, c). Three kinds of interplanar spacings of 2.10 Å and 1.86 Å, 2.09 Å are observed, which are assigned to the (220) plane of cubic Li₂Se (JCPDS No.47-1696) and (200), (111) planes of hexagonal Ni (JCPDS No.45-1027), which are also proved by SAED pattern. In addition, the (210) crystallographic plane with 2.79 Å belongs to unreacted NiSe₂. As the NiSe/NiSe₂@C electrode is gradually charged back to 1.81 V (stage G) and 3.00 V (stage H), the diffraction peaks of Li₂Se are always existed, implying partial irreversible redox reaction during the first cycle. Moreover, the broad peak at 32.8° and weak peak at 36.8° for the fully charged electrode could be assigned to (101) plane of NiSe and (211) plane NiSe₂, respectively, owing to the Li⁺ extraction outside the electrode resulting from the redox between Li₂Se

and metallic Ni⁰. The regeneration of NiSe and NiSe₂ at stage H is also confirmed by HRTEM and SAED (Fig. 6d, e). In addition, the postmortem TEM characterizations show that the NiSe/NiSe₂ domains are consistently anchored into the carbon framework during the whole charge/discharge processes, indicating excellent structural stability of the NiSe/NiSe₂@C (Fig. S13, Supporting Information). Based on the above results, the electrochemical reaction process of the NiSe/NiSe₂@C should be summarized as follows

Discharge:



Charge:



The galvanostatic charge/discharge tests indicate that the NiSe/NiSe₂@C electrode delivers gradually increased reversible capacities at various current densities (Fig. 4). This phenomenon of capacity enhancement is generally attributed to the reversible generation and decomposition of polymeric-gel film [41]. However, the charge/discharge profiles at 0.1 A g⁻¹ clearly show that the reversible capacity after 70 cycles is almost three times than that at third cycle (Fig. 6f). Such conspicuous enhancement of reversible capacity for the NiSe/NiSe₂@C draws our attention to investigate the origin. The differential capacity versus voltage plots from 2 to 70 cycles are depicted in Fig. 6g and h, from which it could be seen that the redox peaks at 1.44

V (cathodic region) and 1.97 V (anodic region) become more and more obvious, and meanwhile a new pair of peaks at 1.67 V/2.21 V emerges with gradually improved intensities upon cycling. This demonstrates that more and more selenides are involved in the electrochemical lithiation/delithiation due to the electrode activation. Moreover, another new pair of peaks appears at 0.75 V (cathodic region) and 1.34 V (anodic region), which should be ascribed to the reversible formation and decomposition of polymeric-gel film on the surface of active materials [9,42]. The enhanced peak intensities should be due to gradual activation of the electrode that continually generates fresh sites, indicating that large amount of Li^+ ions are stored in this way upon repeated cycling.

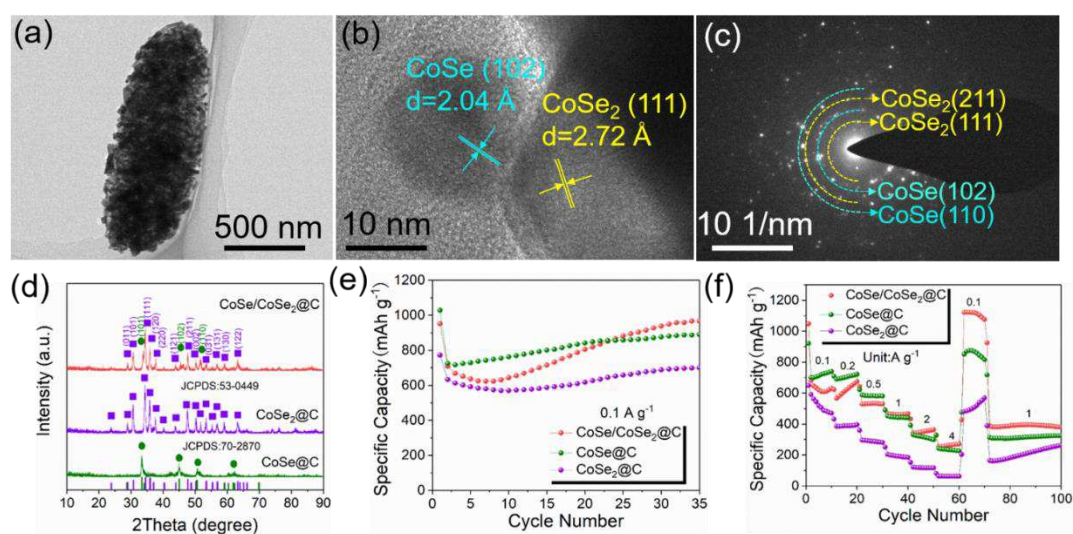


Fig. 7. Characterization and electrochemical performance of the CoSe/CoSe₂@C. (a) TEM image, (b) HRTEM image, and (c) SAED pattern of the CoSe/CoSe₂@C. (d) XRD patterns, (e) cyclic performance at 0.1 A g⁻¹, and (f) rate capabilities of the CoSe@C, CoSe₂@C, and CoSe/CoSe₂@C in LIBs application.

To further demonstrate the superiority of monometallic selenides heterostructure to single-phase selenides, we also prepared CoSe/CoSe₂@C as well as CoSe@C and CoSe₂@C samples under the identical synthetic process (Fig. 7, S14 and S15,

Supporting Information). Fig. 7a shows that the as-prepared CoSe/CoSe₂@C display shuttle-like morphology with numerous heterostructure nanocrystals uniformly embedded into the carbon matrix. HRTEM image reveals the two-phase property of the product with clear heterointerface (Fig. 7b), while the lattice fringes with interplanar spacings of 2.04 and 2.72 Å can be labeled by the (102) plane of CoSe and (111) plane of CoSe₂, respectively. SAED pattern (Fig. 7c) further indicates the coexistence of CoSe₂ and CoSe in the CoSe/CoSe₂@C. XRD pattern (Fig. 7d) shows that the diffraction peaks of CoSe/CoSe₂@C are identified to hexagonal CoSe (JCPDS No. 70-2870) and cubic CoSe₂ (JCPDS No. 53-0449), again confirming the formation of CoSe/CoSe₂ heterostructure. Detailed structural characterization of the CoSe@C and CoSe₂@C are depicted in Fig. S14 and S15. Fig. 7e compares the cyclic performance of the three electrodes at 0.1 A g⁻¹. Clearly, the CoSe/CoSe₂@C exhibited higher reversible capacity of 967.1 mAh g⁻¹ after 35 cycles than CoSe@C (890.4 mAh g⁻¹) and CoSe₂@C (700.3 mAh g⁻¹). Moreover, the CoSe/CoSe₂@C also manifests much superior rate capabilities, delivering reversible capacities of 622.6, 674.9, 529.9, 466.8, 363.5, and 271.3 mAh g⁻¹ at 0.1, 0.2, 0.5, 1.0, 2.0, 4.0 A g⁻¹, respectively (Fig. 7f). When the current density is restored to 0.1 A g⁻¹, the average capacity reaches back to 1076.4 mAh g⁻¹. The above results once again prove the advantages of monometallic heterostructure over single-phase materials towards LIBs application.

4. Conclusions

In summary, the monometallic selenides heterostructures surrounded by conductive carbon matrix (NiSe/NiSe₂@C, CoSe/CoSe₂@C) were synthesized, by

adjusting the ratio of MOF precursor to selenium powder during calcination. The heterostructure materials manifest superior electrochemical performance to their single-phase counterparts as anodes for LIBs. Specially, the NiSe/NiSe₂@C delivers high reversible capacity (1015.5 at 0.1 A g⁻¹), excellent rate capability (500.8 at 4 A g⁻¹), and long-term cyclic stability (540.3 mAh g⁻¹ after 1000 cycles at 1 A g⁻¹). This enhanced lithium storage properties should be due to the heterogeneous interface between NiSe and NiSe₂ domains with electrons rearrangement, which promotes rapid charge transfer and ion adsorption, as well as increases the electrochemically active sites, thus improving the reaction kinetics. EIS, GITT, and kinetics analysis further demonstrate that the NiSe/NiSe₂@C possesses lower charge transfer resistance, faster diffusion coefficient of Li⁺ ions, and more favored capacitive energy. Besides, the porous carbon skeleton in-situ converted from Ni-MOF not only increases the electrical conductivity of the material, but also provides abundant channel for the infiltration of electrolyte. We anticipate the present strategy for engineering two-phase heterostructure with single cations and single anions could be extended to other compounds for various applications.

Acknowledgements

We gratefully acknowledge financial supports from the Natural Science Foundation of Shandong Province (No. ZR2020QE066), Taishan Scholar Project (No. ts201511080), the fellowship of China Postdoctoral Science Foundation (No. 2020M672081), Opening Project of State Key Laboratory of Advanced Technology for Float Glass (No.

2020KF08), and Laboratory Construction Project of Shandong University of Technology (No. 2019007).

Electronic Supplementary Material

Supplementary material is available in the online version of this article at <https://doi.org/10.1007/s40145-...>

References

- [1] M. Zhong, Li. Kong, N. Li, *et al.* Synthesis of MOF-derived nanostructures and their applications as anodes in lithium and sodium ion batteries, *Coordin. Chem. Rev.* 388 (2019) 172-201, <https://doi.org/10.1016/j.ccr.2019.02.029>.
- [2] E. M. Erickson, C. Ghanty, D. Aurbach, New Horizons for Conventional Lithium Ion Battery Technology, *J. Phys. Chem. Lett.* 5 (2014) 3313-3324, [10.1021/jz501387m](https://doi.org/10.1021/jz501387m).
- [3] D. Nan, Z.-H. Huang, F.-Y. Kang, *et al.* Research progress on fibrous carbon materials as anode materials for lithium ion batteries, *Carbon* 86 (2015) 371-374, [10.1016/j.carbon.2015.02.002](https://doi.org/10.1016/j.carbon.2015.02.002).
- [4] M. Srinivaas, C.-Y. Wu, J.-G. Duh, *et al.* Highly Rich 1T Metallic Phase of Few-Layered WS₂ Nanoflowers for Enhanced Storage of Lithium-Ion Batteries, *ACS Sustain. Chem. Eng.* 7(2019) 10363-10370, [10.1021/acssuschemeng.9b00351](https://doi.org/10.1021/acssuschemeng.9b00351).
- [5] X. Zhang, J. Zhou, Y. Zheng, *et al.* MoSe₂-CoSe₂/N-doped graphene aerogel nanocomposites with high capacity and excellent stability for lithium-ion batteries, *J. Power Sources* 439 (2019) 227112, [10.1016/j.jpowsour.2019.227112](https://doi.org/10.1016/j.jpowsour.2019.227112).

- [6] S. Li, Y. Liu, P. Guo, et al. Self-Climbed Amorphous Carbon Nanotubes Filled with Transition Metal Oxide Nanoparticles for Large Rate and Long Lifespan Anode Materials in Lithium Ion Batteries, *ACS Appl. Mater. Inter.* 9 (2017) 26818-26825, 10.1021/acsami.7b06394.
- [7] Z. Hu, Q. Liu, S. -L. Chou, et al. Advances and Challenges in Metal Sulfides/Selenides for Next-Generation Rechargeable Sodium-Ion Batteries, *Adv. Mater.* 29 (2017) 1700606, 10.1002/adma.201700606.
- [8] D. Ma, Q. Zhu, X. Li, *et al.* Unraveling the Impact of Ether and Carbonate Electrolytes on the Solid-Electrolyte Interface and the Electrochemical Performances of ZnSe@C Core-Shell Composites as Anodes of Lithium-Ion Batteries, *ACS Appl. Mater. Inter.* 11(2019) 8009-8017, 10.1021/acsami.8b21237.
- [9] G. D. Park, J. H. Hong, S.-K. Park, et al. Strategy for synthesizing mesoporous NiO polyhedra with empty nanovoids via oxidation of NiSe polyhedra by nanoscale Kirkendall diffusion and their superior lithium-ion storage performance, *App. Surf. Sci.* 464 (2019) 597-605, 10.1016/j.apsusc.2018.09.122.
- [10] Q. Wang, M. Hou, D. Liu, *et al.* Mechanism and improvement strategy of CoSe capacity change during lithiation/delithiation, *J. Alloy. Compd.* 26 (2021) 158099, 10.1016/j.jallcom.2020.158099.
- [11] X. Xiao, L. Ni, G. Chen, *et al.* Two-dimensional NiSe₂ nanosheets on carbon fiber cloth for high-performance lithium-ion batteries, *J. Alloy. Compd.* 821 (2020) 153218, 10.1016/j.jallcom.2019.153218.

- [12] X. Zhang, J. Zhou, Y. Zheng, et al. Co_{0.85}Se Nanoparticles Encapsulated by Nitrogen-Enriched Hierarchically Porous Carbon for High-Performance Lithium-Ion Batteries, *ACS Appl. Mater. Inter.* 12 (2020) 9236-9247, 10.1016/j.jallcom.2019.153218.
- [13] M. H. Yap, K. L. Fow, G. Z. Chen, Synthesis and applications of MOF-derived porous nanostructures, *Green Energy Environ.* 2 (2017) 218-245, 10.1016/j.gee.2017.05.003.
- [14] D. Adekoya, S. Zhang, M. Hankel, 1D/2D C₃N₄/Graphene Composite as a Preferred Anode Material for Lithium Ion Batteries: Importance of Heterostructure Design via DFT Computation, *ACS Appl. Mater. Inter.* 12 (2020) 25875-25883, 10.1021/acsami.0c04900.
- [15] C. Zhao, X. Wang, J. Kong, et al. Self-Assembly-Induced Alternately Stacked Single-Layer MoS₂ and N-doped Graphene: A Novel van der Waals Heterostructure for Lithium-Ion Batteries, *ACS Appl. Mater. Inter.* 8 (2016) 2372-2379, 10.1021/acsami.0c04900.
- [16] G. Fang, Q. Wang, J. Zhou, et al. Metal Organic Framework-Templated Synthesis of Bimetallic Selenides with Rich Phase Boundaries for Sodium-Ion Storage and Oxygen Evolution Reaction, *ACS Nano* 13 (2019) 5635-5645, 10.1021/acsnano.9b00816.
- [17] K. Chen, X. Wang, G. Wang, et al. A new generation of high performance anode materials with semiconductor heterojunction structure of SnSe/SnO₂@Gr in lithium-ion batteries, *Chem. Eng. J.* 347 (2018) 552-562,

10.1016/j.cej.2018.04.125.

- [18] X. Li, S. Zheng, L. Jin, *et al.* Metal-Organic Framework-Derived Carbons for Battery Applications, *Adv. Energy Mater.* 8 (2018) 1800716, 10.1002/aenm.201800716.
- [19] H. Lin, X. Jin, N. Lou, *et al.* Metallic VS₂/blue phosphorene heterostructures as promising anode materials for high-performance lithium ion batteries: A first principles study, *Appl. Surf. Sci.* 533 (2020) 147478, 10.1016/j.apsusc.2020.147478.
- [20] F. Wang, Y. Li, T. A. Shifa, *et al.* Selenium-Enriched Nickel Selenide Nanosheets as a Robust Electrocatalyst for Hydrogen Generation, *Angew. Chem. Int. Edit.* 55 (2016) 6919-6914, <https://doi.org/10.1002/anie.201602802>.
- [21] Y. He, M. Luo, C. Dong, *et al.* Coral-like Ni_xCo_{1-x}Se₂ for Na-ion battery with ultralong cycle life and ultrahigh rate capability, *Mater. Chem. A* 7 (2019) 3933-3940, 10.1039/c8ta10114k.
- [22] W. Shi, X. Zhang, G. Che, Hydrothermal synthesis and electrochemical hydrogen storage performance of porous hollow NiSe nanospheres, *Int. J. Hydrogen Energ.* 38 (2013) 7037-7045, 10.1016/j.ijhydene.2013.03.145.
- [23] Z. Ran, C. Shu, Z. Hou, *et al.* Ni₃Se₂/NiSe₂ heterostructure nanoforests as an efficient bifunctional electrocatalyst for high-capacity and long-life Li-O₂ batteries, *J. Power Sources* 468 (2020) 228308, 10.1016/j.jpowsour.2020.228308.
- [24] Z. Zou, X. Wang, J. Huang, *et al.* An Fe-doped nickel selenide nanorod/nanosheet

- hierarchical array for efficient overall water splitting, *J. Mater. Chem. A* 7 (2019) 2233-2341, 10.1016/j.jpowsour.2020.228308.
- [25] C. Chen, Y. Huang, Z. Meng, *et al.* Hexagonal prism structured MnSe stabilized by nitrogen-doped carbon for high performance lithium ion batteries, *J. Mater. Sci. Technol.* 76 (2021) 11-19, 10.1016/j.jmst.2020.11.014.
- [26] X. Liang, B. Zheng, L. Chen, *et al.* Template directed hydrothermal synthesis of flowerlike NiSe_x/C composites as lithium/sodium ion battery anodes, *ACS Appl. Mater. Inter.* 9 (2017) 23222-23229, 10.1021/acsami.7b06152.
- [27] J. Yang, N. Yang, Q. Xu, *et al.* Bioinspired Controlled Synthesis of NiSe/Ni₂P Nanoparticles Decorated 3D Porous Carbon for Li/Na Ion Batteries, *ACS Sustain. Chem. Eng.* 7 (2019) 13217-13225, 10.1021/acssuschemeng.9b02478.
- [28] X. Xiao, D. Huang, Y. Fu, *et al.* Engineering NiS/Ni₂P Heterostructures for Efficient Electrocatalytic Water Splitting, *ACS Appl. Mater. Inter.* 10 (2018) 4689-4696, 10.1021/acssuschemeng.9b02478.
- [29] Z. Huang, B. Xu, Z. Li, *et al.* Accurately Regulating the Electronic Structure of Ni_xSe_y@NC Core-Shell Nanohybrids through Controllable Selenization of a Ni-MOF for pH-Universal Hydrogen Evolution Reaction, *Small* 16 (2020) e2004231, 10.1002/sml.202004231.
- [30] R. Liang, C. Shu, A. Hu, *et al.* Interface engineering induced selenide lattice distortion boosting catalytic activity of heterogeneous CoSe₂@NiSe₂ for lithium-oxygen battery, *J.* 393 (2020) 124592, 10.1016/j.cej.2020.124592.
- [31] H. Luo, B. Wang, C. Wang, *et al.* Synergistic deficiency and heterojunction

- engineering boosted VO₂ redox kinetics for aqueous zinc-ion batteries with superior comprehensive performance, *Energy Storage Mater.* 33 (2020) 390-398, 10.1016/j.ensm.2020.08.011.
- [32] X. Zhu, S. Li, J. Li, *et al.* Free-standing WTe₂QD-doped NiSe/C nanowires for highly reversible lithium storage, *Electrochim. Acta.* 295 (2019) 22-28, 10.1016/j.electacta.2018.10.128.
- [33] J. S. Cho, S. Y. Lee, Y. C. Kang. First Introduction of NiSe₂ to Anode Material for Sodium-Ion Batteries: A Hybrid of Graphene-Wrapped NiSe₂/C Porous Nanofiber, *Sci Rep.* 6 (2016) 23338, 10.1038/srep23338.
- [34] S. Fan, G. Li, G. Yang, *et al.* NiSe₂ nanooctahedra as anodes for high-performance sodium-ion batteries, *New J. Chem.* 43 (2019) 12858-12864, 10.1039/c9nj02631b.
- [35] P. Liu, J. Han, K. Zhu, *et al.* Heterostructure SnSe₂/ZnSe@PDA Nanobox for Stable and Highly Efficient Sodium-Ion Storage, *Adv. Energy Mater.* 10 (2020) 2000741, 10.1002/aenm.202000741.
- [36] D. Cao, W. Kang, W. Wang, *et al.* Okra-Like Fe₇S₈/C@ZnS/N-C@C with Core-Double-Shelled Structures as Robust and High-Rate Sodium Anode, *Small* 16 (2020) 1907641, 10.1002/smll.201907641.
- [37] D. Chen, S. Sun, G. Yu, *et al.* Coaxial structure of NiFe₂O₄/CNTs composites as anodes for enhanced lithium ion batteries, *J. Chen, Carbon* 166 (2020) 91-100, 10.1016/j.carbon.2020.05.008.
- [38] C. Dong, L. Guo, H. Li, *et al.* Rational fabrication of CoS₂/Co₄S₃@N-doped carbon

- microspheres as excellent cycling performance anode for half/full sodium ion batteries, *Energy Storage Mater.* 25 (2020) 679-686, 10.1016/j.ensm.2019.09.019.
- [39] T. Yang, J. Liu, D. Yang, *et al.* Bi₂Se₃@C Rod-like Architecture with Outstanding Electrochemical Properties in Lithium/Potassium-Ion Batteries, *ACS Appl. Energ. Mater.* 3 (2020) 11073-11081, 10.1021/acsaem.0c02056.
- [40] X. Ou, J. Li, F. Zheng, *et al.* In situ X-ray diffraction characterization of NiSe₂ as a promising anode material for sodium ion batteries, *J. Power Sources* 343 (2017) 483-491, 10.1016/j.jpowsour.2017.01.097.
- [41] D. Wang, R. Zhang, J. Li, *et al.* General synthesis of graphene-supported bicomponent metal monoxides as alternative high-performance Li-ion anodes to binary spinel oxides, *J. Mater. Chem. A* 5 (2017) 1687-1697, 10.1039/c6ta07936a.
- [42] Z. Liu, X.-Y. Yu, U. Paik, Etching-in-a-Box: A Novel Strategy to Synthesize Unique Yolk-Shelled Fe₃O₄@Carbon with an Ultralong Cycling Life for Lithium Storage, *Adv. Energy Mater.* 6 (2016) 1502318, 10.1002/aenm.201502318.

Figures

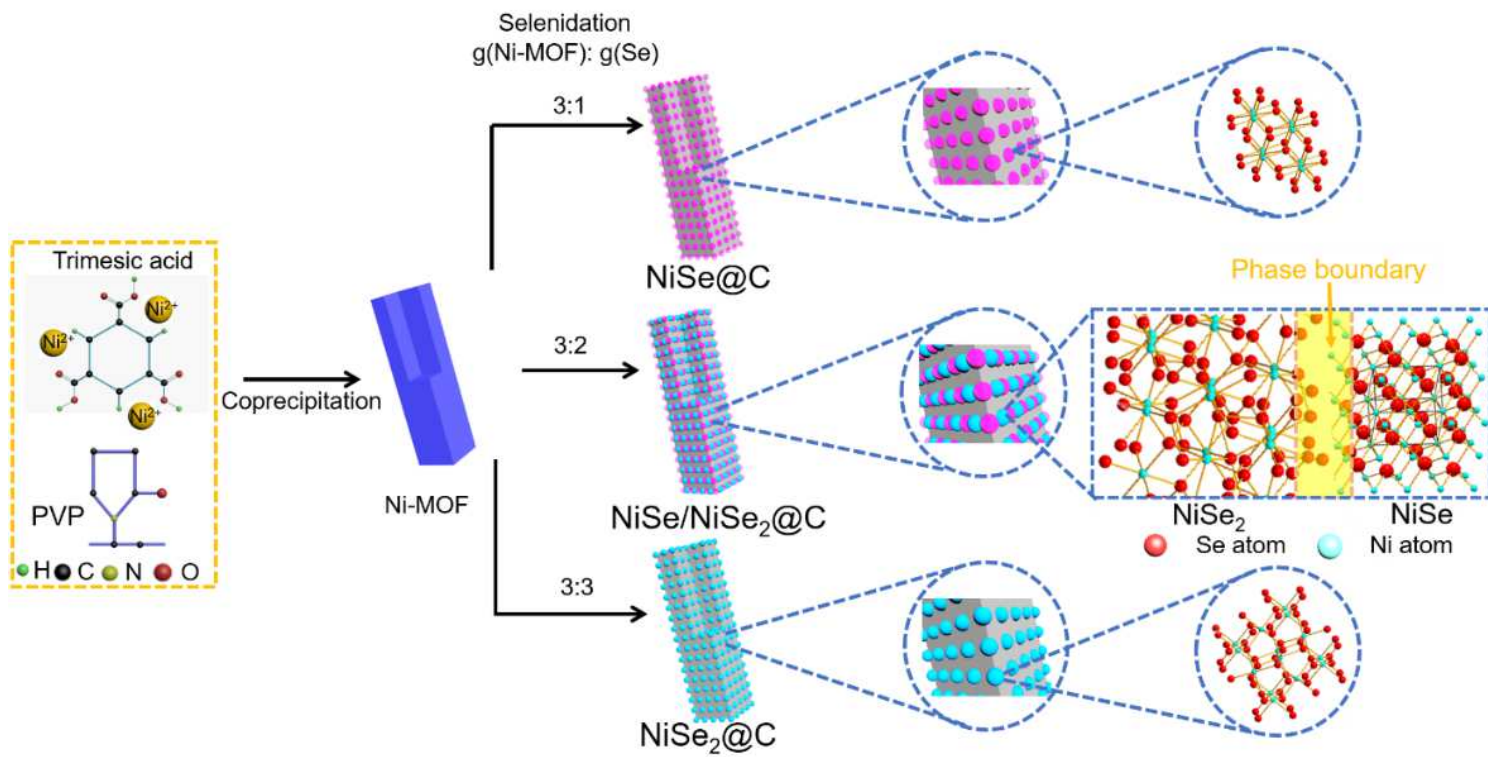


Figure 1

Schematic illustration for the preparation process of the $\text{NiSe}@C$, $\text{NiSe}/\text{NiSe}_2@C$, and $\text{NiSe}_2@C$.

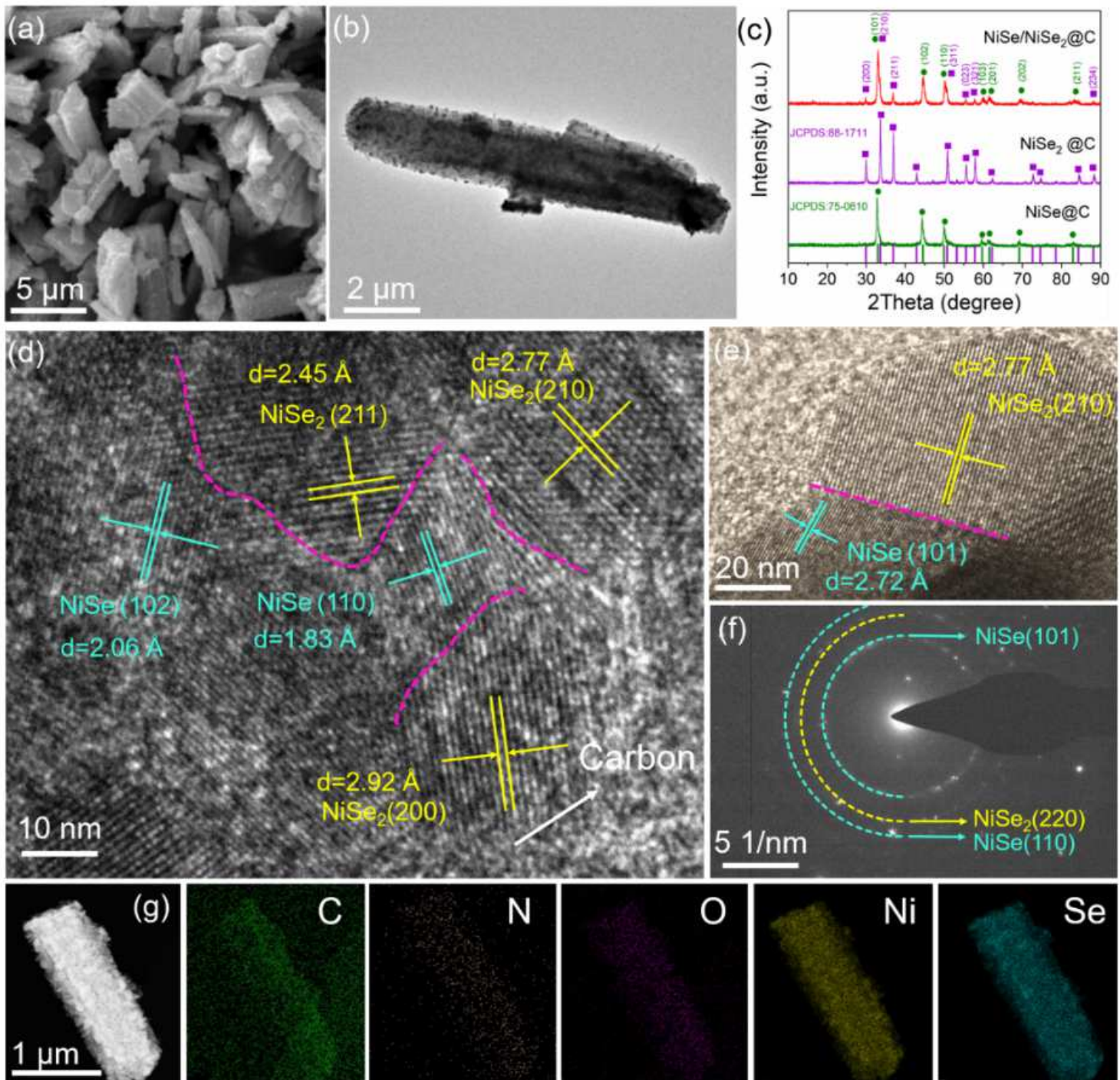


Figure 2

Material characterization. (a) SEM and (b) TEM images of the NiSe/NiSe₂@C. (c) XRD patterns of the NiSe/NiSe₂@C, NiSe@C, and NiSe₂@C. (d, e) HRTEM images, (f) SAED pattern, (g) HAADF-STEM and elemental mappings images (Ni, Se, C, N, O) of the NiSe/NiSe₂@C.

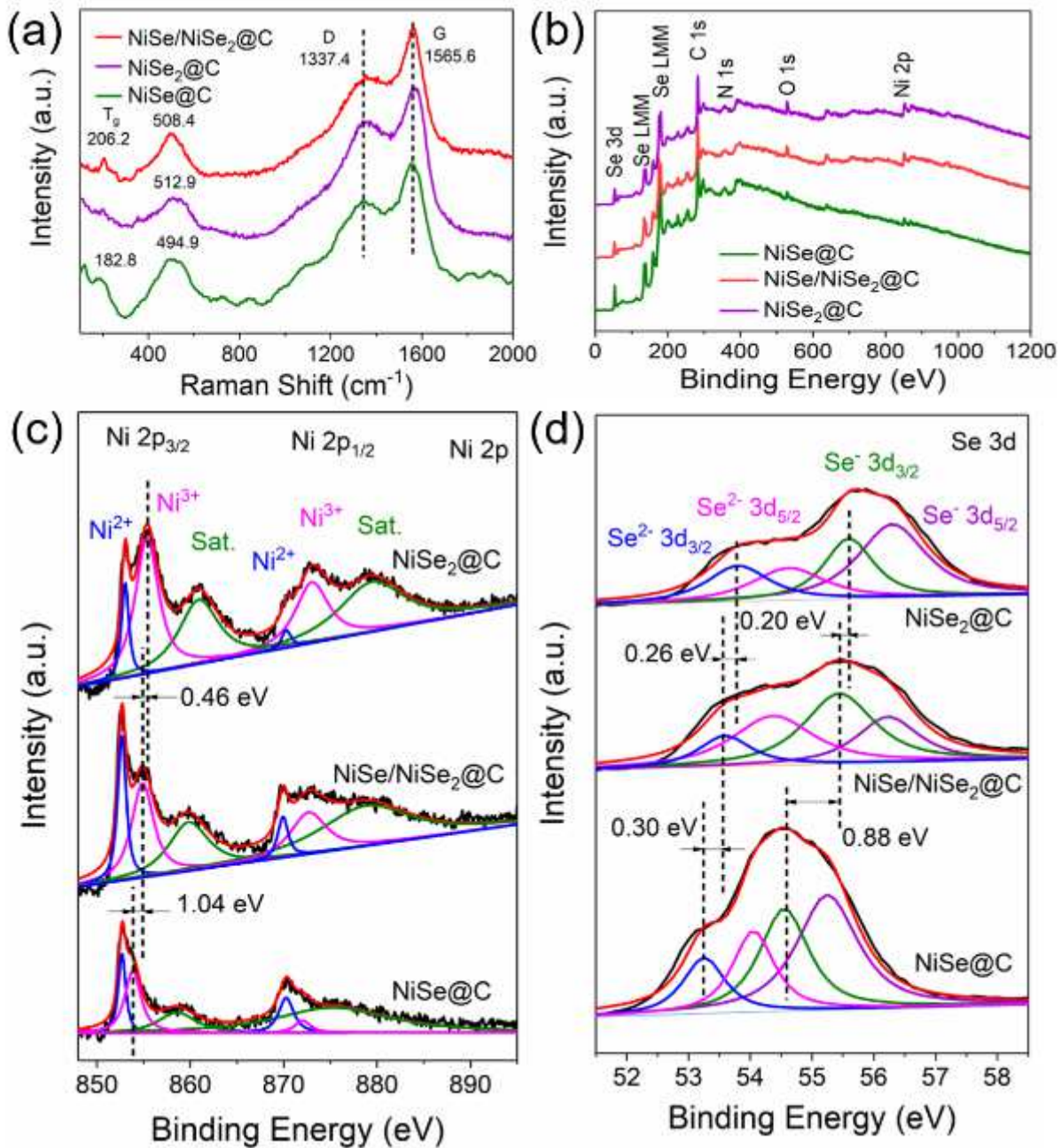


Figure 3

Material characterization. (a) Raman spectra of the NiSe/NiSe₂@C, NiSe@C, and NiSe₂@C. (b) The survey XPS spectra of the NiSe/NiSe₂@C, NiSe@C, and NiSe₂@C. (c) Comparison of high-resolution Ni 2p XPS spectra for the NiSe/NiSe₂@C and NiSe@C, and for the NiSe/NiSe₂@C and NiSe₂@C. (d) Comparison of high-resolution Se 3d XPS spectra for the NiSe/NiSe₂@C and NiSe@C, and for (f) the NiSe/NiSe₂@C and NiSe₂@C.

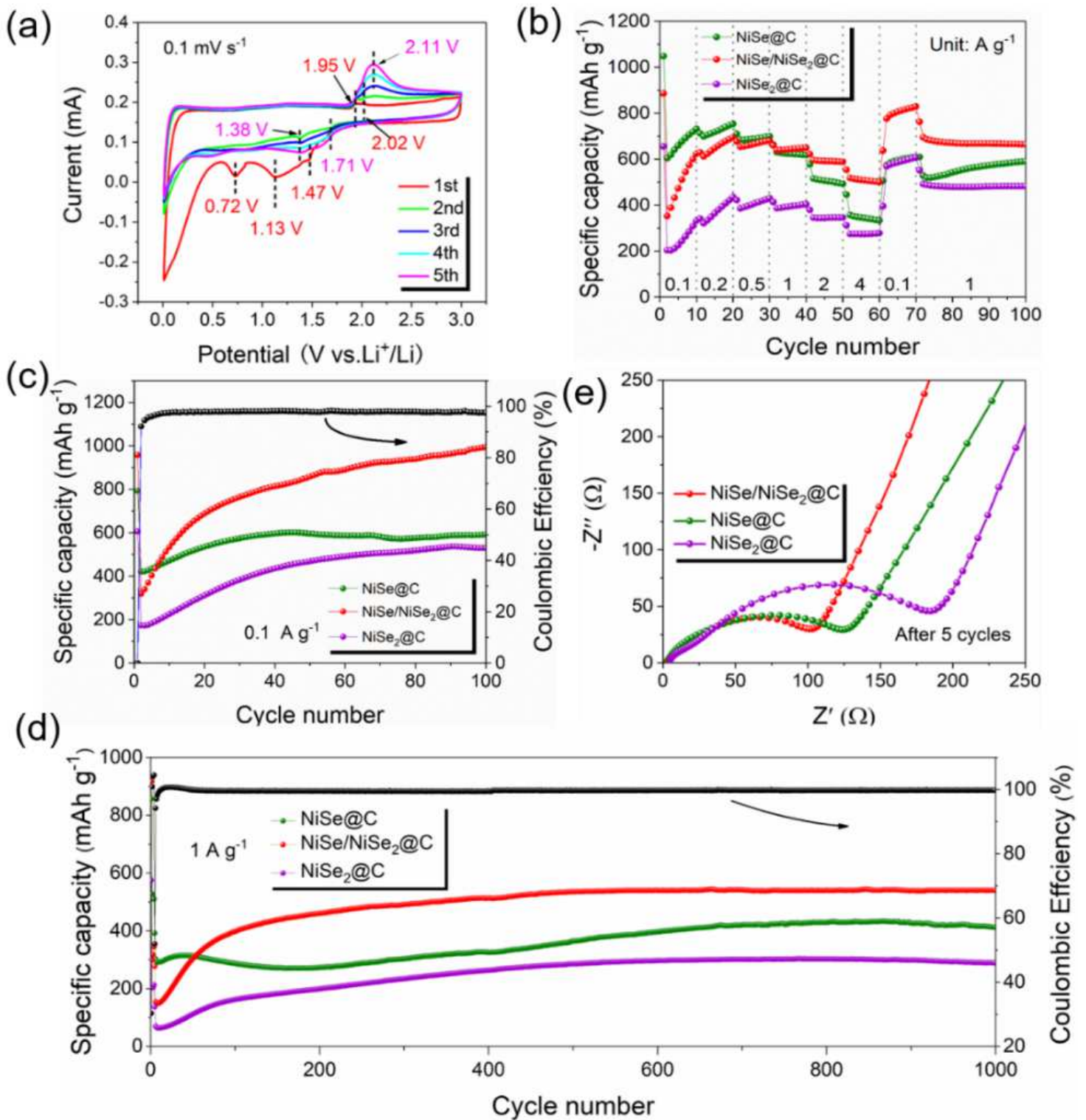


Figure 4

Lithium storage properties. (a) First five CV curves of the NiSe/NiSe₂@C at 0.1 mV s⁻¹. (b) Rate capabilities of the NiSe/NiSe₂@C, NiSe@C, and NiSe₂@C. Cyclic performance of the NiSe/NiSe₂@C, NiSe@C, and NiSe₂@C at (c) 0.1 A g⁻¹ and (d) 1 A g⁻¹. (e) Nyquist plots of the NiSe/NiSe₂@C, NiSe@C, and NiSe₂@C after 5 charge/discharge cycles.

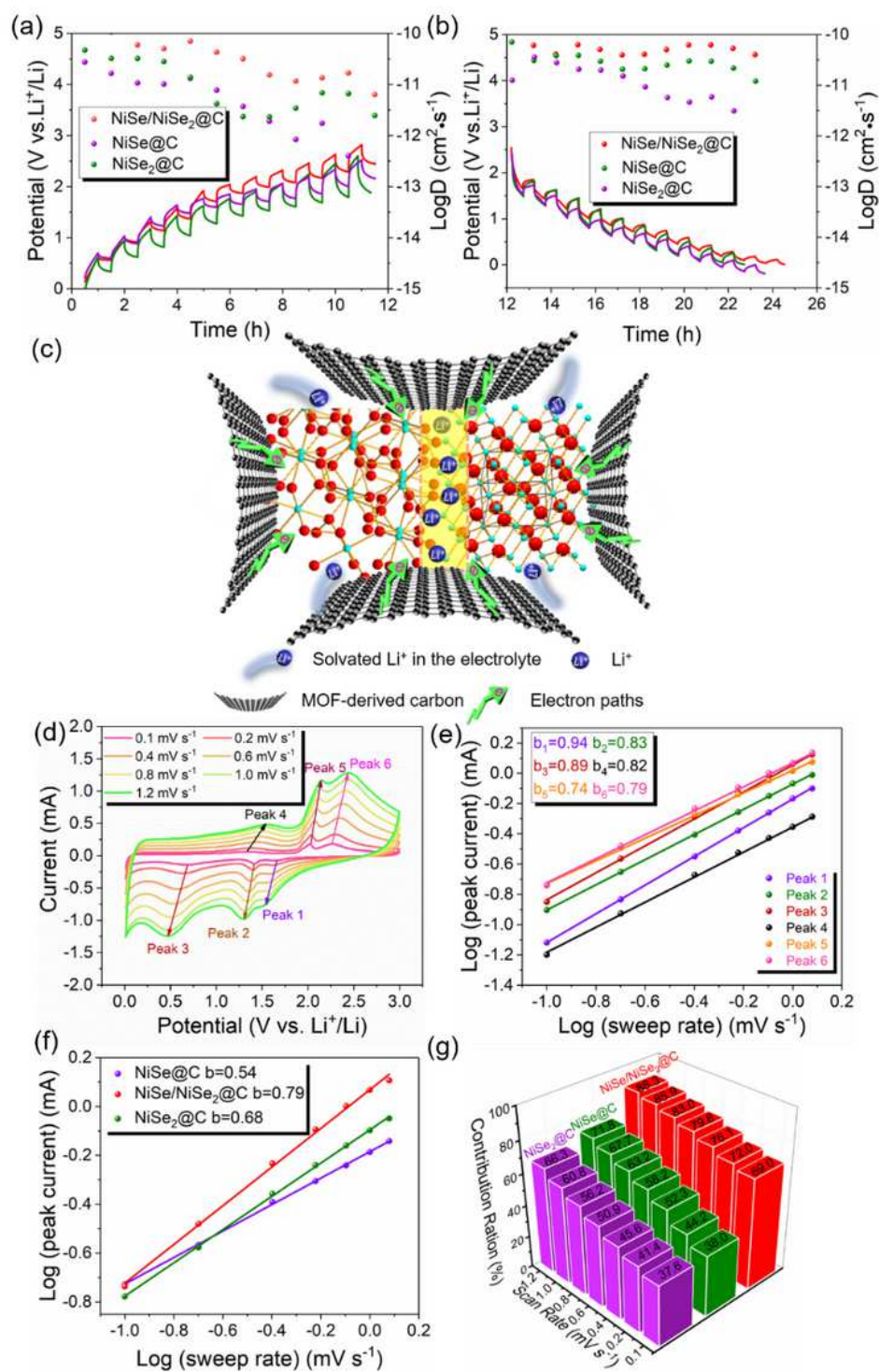


Figure 5

Kinetics analyses. GITT curves and corresponding Li⁺ ions diffusion coefficients of the NiSe/NiSe₂@C, NiSe@C, and NiSe₂@C electrodes during (a) the 10th discharge process and (b) the 10th charge process. (c) Schematic illustration for the charge storage of the NiSe/NiSe₂@C. (d) CV curves of the NiSe/NiSe₂@C at various scan rates from 0.1 to 1.2 mV s⁻¹ after 5 charge/discharge cycles. (e) Linear relationship between log (i) and log (v) of the NiSe/NiSe₂@C. (f) Comparison of b values among the

NiSe/NiSe₂@C, NiSe@C, and NiSe₂@C electrodes. (g) The percentage of capacitive contributions at different scan rates of the NiSe/NiSe₂@C, NiSe@C, and NiSe₂@C electrodes.

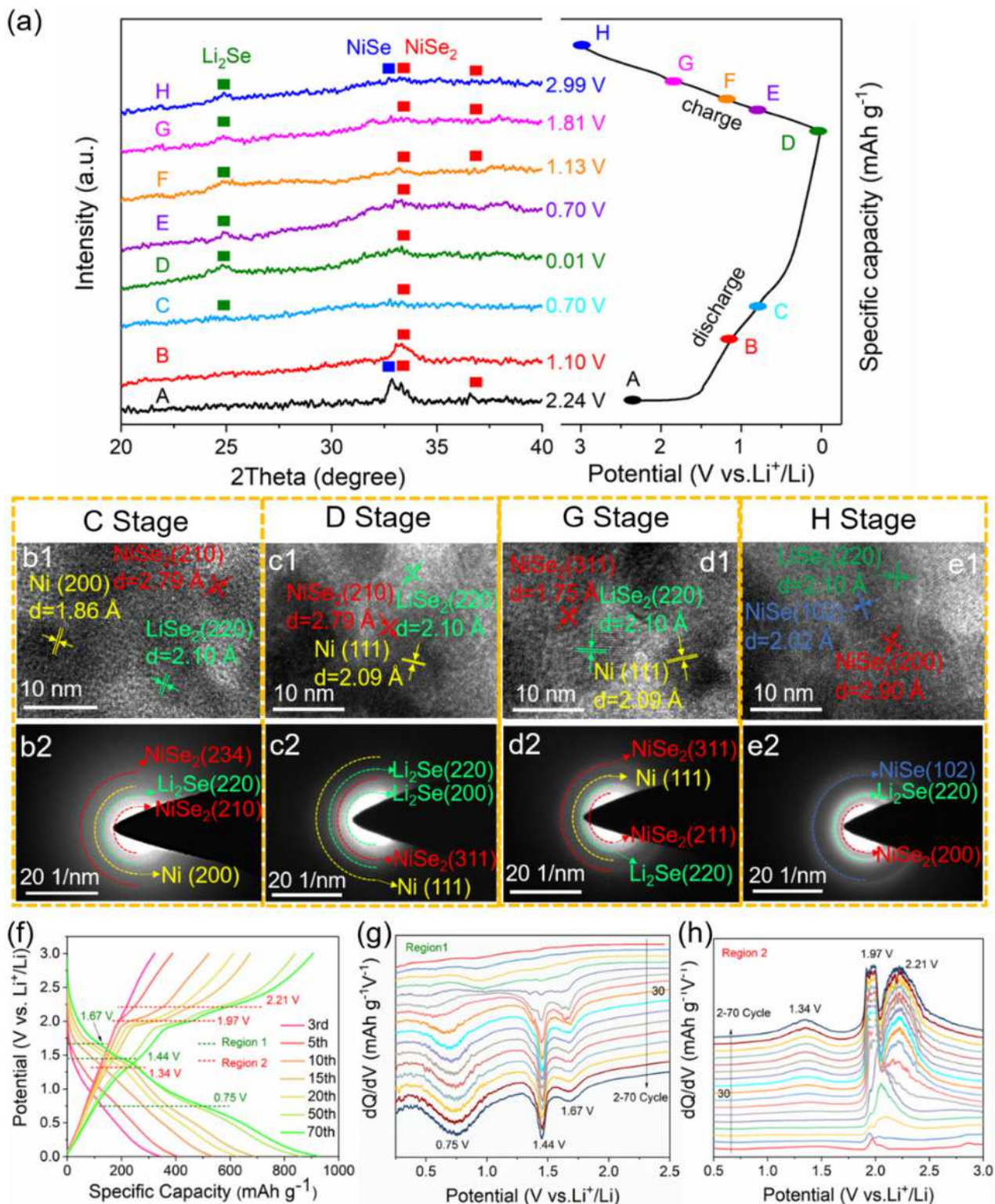


Figure 6

Electrochemical reaction mechanism. (a) Ex-situ XRD patterns collected at different cut-off voltages, corresponding to the charge/discharge curves. Ex-situ HRTEM images and corresponding SAED patterns of the NiSe/NiSe₂@C electrode at C stage (b1-b2), D stage (c1-c2), G stage (d1-d2), and H stage (e1-e2)

during the first cycle. (f) Representative charge–discharge voltage profiles of the NiSe/NiSe₂@C electrode with corresponding differential capacity versus voltage plots at (g) region 1 (discharge) and (h) region 2 (charge).

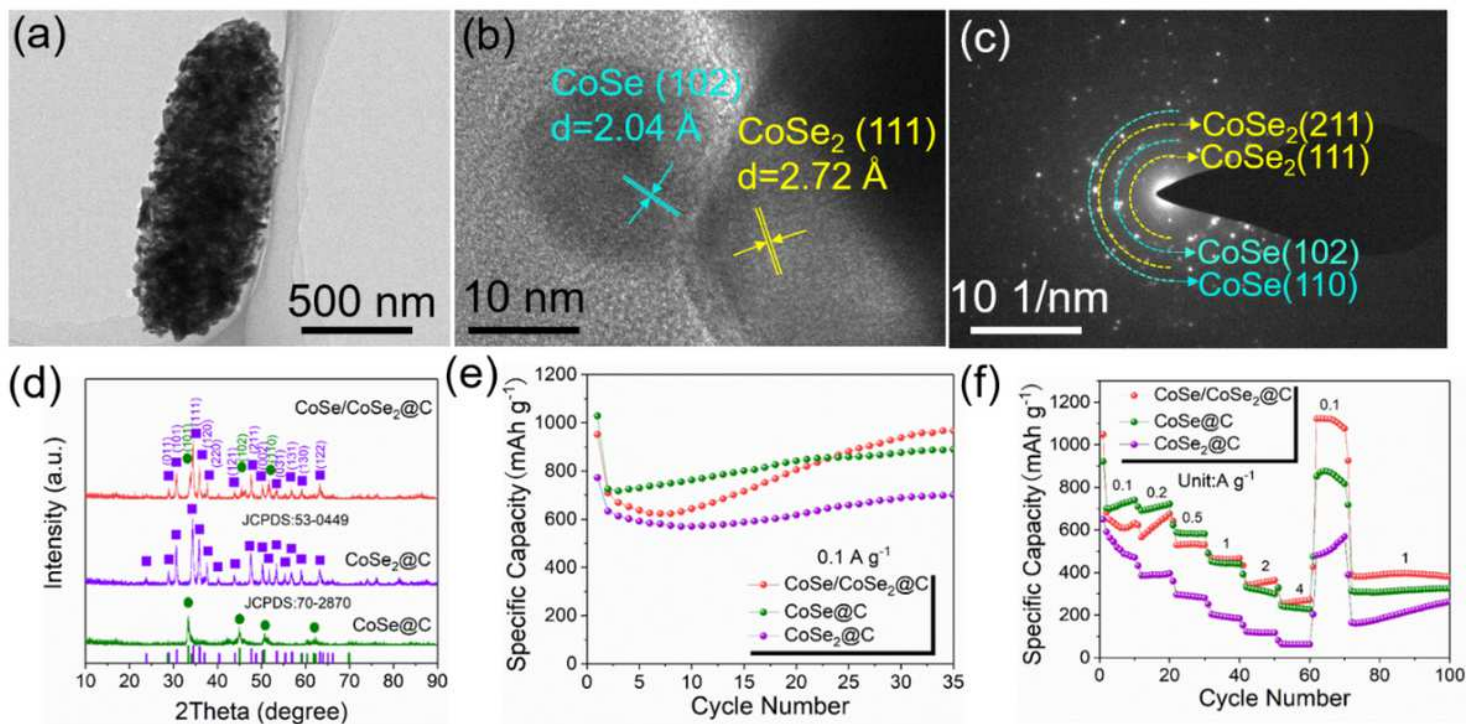


Figure 7

Characterization and electrochemical performance of the CoSe/CoSe₂@C. (a) TEM image, (b) HRTEM image, and (c) SAED pattern of the CoSe/CoSe₂@C. (d) XRD patterns, (e) cyclic performance at 0.1 A g⁻¹, and (f) rate capabilities of the CoSe@C, CoSe₂@C, and CoSe/CoSe₂@C in LIBs application.

Supplementary Files

This is a list of supplementary files associated with this preprint. Click to download.

- [JACSupplementarymaterialsLiu5.1.docx](#)